Requirements and Tests for Phase Preservation in a SAR Processor

Michele Belotti, Davide D'Aria, Pietro Guccione, Nuno Miranda, Andrea Monti Guarnieri, *Member, IEEE*, and Betlem Rosich

I. Introduction

THE accurate estimation of deformations and the generation of digital elevation models and tomography are among the best achievements of synthetic aperture radar (SAR) interferometry (InSAR). InSAR relies on the phase difference of complex images of the same target acquired at different positions and/or times. To obtain accurate results, the phase preservation throughout the whole acquisition and processing chain is of paramount importance. In this chain, focusing is one of the most challenging tasks as it requires a space-variant kernel to be implemented with the highest efficiency. There is a widespread and still growing literature on the design of FFT-based focusing kernel for very different systems, monostatic and bistatic, intended for spaceborne or airborne data and in very different acquisition modes.

The phase-preserving approaches introduced by the majority of these papers evidence the quality of the method by measurements based on the focused point target, which may be enough to prove the concept but not to compare such quality with that achieved by other schemes [1]. A quantitative "phase-preserving" test, canonically accepted in the SAR community and named "CEOS offset test" [2], [3], has been devoted to such purpose. Basically, the CEOS offset test aims at verifying and assessing the phase preservation of a focusing processor. The phase accuracy in a processor is of paramount importance, and the idea of testing it by the creation of autointerferogram was originally suggested by Raney and Bamler [4]. In such test, the same scene, either simulated or real, is shifted by an integer number of pixels in range/azimuth and is passed through the processing system. An interferogram made with the two complex products can be used to reveal phase discontinuities and processor noise. Although created to work on images from a single processor, CEOS offset test has also been used to verify the cross-compatibility of SLC products generated by different processors [5]. The CEOS offset test is, however, inadequate in capturing some artifacts in the implementation of the space-variant focusing kernel, and its applicability is currently limited to StripMAP acquisition geometries, as it is tailored to this specific spectral support.[1]

The aim of this paper is to fill this gap by defining a series of quantitative phase-preserving tests in addition to the necessary check for the impulse response function (IRF); [on spatial resolution, peak sidelobe ratio (PSLR), and integrated sidelobe ratio (ISLR)] [7]. These tests are a necessary step to evaluate the performance of different focusing algorithms and to validate the efficiency and precision of the processors compared to some necessary conditions. In the test's description, attention has been paid in defining the test and the measurement procedures to cover a wide variety of acquisition modes, systems, and geometries (which can include, even if not expressly mentioned, airborne, spaceborne, and ground-based systems, and monostatic and bistatic configurations). The difference of this paper from [8] and [9], where the need to introduce these tests has been formerly discussed, is that here a more formal derivation of the requirements and of the test procedure is treated.

This paper is outlined as follows.

1) Section II proposes the high-level requirements for interferometric applications for both single- or repeat-pass configurations.
2) Section III presents the different acquisition modes considered in this paper.
3) Section IV proposes and describes the different phase tests.
4) Section V discusses the pertinence of the tests to each acquisition mode.

Manuscript received June 3, 2011; revised December 6, 2011, June 8, 2012, November 13, 2012, and January 7, 2013; accepted April 17, 2013. Date of publication July 4, 2013; date of current version February 27, 2014.

M. Belotti and A. Monti Guarnieri are with the Politecnico di Milano, 20133 Milan, Italy (e-mail: monti@elet.polimi.it).

D. D'Aria is with Aresys, 20134 Milan, Italy.

P. Guccione is with the Politecnico di Bari, 70125 Bari, Italy.

N. Miranda and B. Rosich are with the European Space Agency, 00044 Frascati, Italy.

Color versions of one or more of the figures in this paper are available online.

[1] In some cases, the CEOS offset test has been applied with success to other acquisition modes (e.g., see [6]).

II. Requirements for Interferometric Applications

In the framework of SAR focusing techniques, the signal-to-noise ratio (SNR) is the universally adopted measure for assessing quality performances. However, in interferometric applications, the standard deviation of the interferometric phase is the quantity to be optimized. In the case of classical DInSAR, the Cramér–Rao bound for the standard deviation of the phase estimation is expressed as follows [10]:

$$\sigma_\phi^2 = \frac{1-\gamma}{\gamma^2 L}\frac{N\gamma-\gamma+1}{2N} \tag{1}$$

where L (with $L>1$) is the set of pixels of a target that is homogeneous and not decorrelating with time in a stack of N images and assuming white independent noise (that holds for quantization). The coherence γ is related to the signal-to-total-noise ratio (STNR), where noise is mainly due to clutter rather than to thermal and quantization

$$\gamma = \frac{1}{1+\mathrm{STNR}^{-1}}. \tag{2}$$

Several different causes impact on the interferometric quality [11], [12], like volumetric effects, temporal decorrelation, and atmospheric phase screen, besides the mentioned thermal, quantization, and clutter noises. All of these contributions are analyzed in case of single-pass and repeat-pass interferometries.

A. Single-Pass Interferometry

For **single-pass** interferometric systems, we can derive requirements either from the current TanDEM-X [13] topographic mission or the future Ka-band SAR-altimeter GLISTIN [14]. In both cases, thermal noise is the major limitation; for example, in the TanDEM-X mission, the target SNR is >16 dB, corresponding to a coherence $\gamma > 0.98$ and a phase accuracy $\sigma_\phi < 9^\circ$, according to (1) and (2). In the latter case, an overall phase error of 5° is required instead. Then, we impose that the phase error standard deviation introduced by focusing is negligible when $\sigma_\phi \ll 5^\circ$. The impact of phase decorrelation in an interferogram is mitigated if the same phase error is repeated in both images [12], which is the case when images are acquired under the same geometry, i.e., a *small* baseline and the same processor and configuration are used. By this point of view, it makes sense to **keep the CEOS offset test requirements**, in both the phase accuracy and bias, to assure, respectively, $\sigma_\phi \leq 5.5^\circ$ and $\phi \leq 0.1^\circ$. It is worthy to remark that the bias is roughly half of the residual phase noise after averaging over the CEOS processing block of 100×100 pixels.

B. Repeat-Pass Interferometry

In case of a **repeated-pass** interferometric system, we have to account for possible larger baselines and additional contributions of scene decorrelation and phase errors due to propagation in the atmosphere. Temporal correlation is higher at lower bands, like in L and C. In C-band, a model for temporal coherence in suburban areas was performed by using data sets acquired by ERS-1 and ERS-2 with a repeat pass of just three days [15], [16]. The short-lag interferometric coherence was estimated by summing coherently subsequent interferograms after the removal of their average phase. The corresponding histogram of the phase standard deviation [as in (1)] is shown in Fig. 1. Almost all of the pixels have short-term coherence well below 0.99 ($\sigma_\phi < 0.2^\circ$): For these pixels, the *added* -20 dB *noise leads to measurable quality worsening*, and therefore, it could be a limiting effect. As 20 dB would correspond to a phase standard deviation of $\sigma_\phi = 5.7^\circ$, it is desirable to keep the processor noise well below this value.

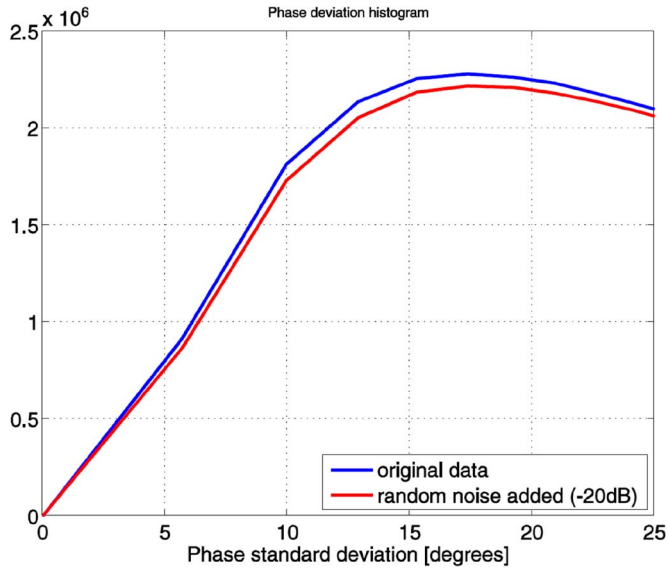

Fig. 1. Short-lag phase deviation histogram from the three-day revisit data set acquired during ERS ICE phase, suburban area of Rome (blue line). The red line shows the effect of adding noise with relative power of -20 dB.

Nonetheless, *it is the large baseline case that is the one most affected by differential phase errors in focusing*, and this is, indeed, the context of a persistent scatterer (PS) analysis [17]. As PSs are loosely affected by scene decorrelation (by definition of PS), as well as thermal and quantization noise (the PSs are, in most cases, strongly reflective point scatterers), the limiting error sources are the phase shifts due to the tropospheric turbulence [18], [19] (assuming to ignore the additional ionospheric noise that affects only L and lower bands). In [20], it has been shown that the residual tropospheric noise in C-band can be reduced to $\sigma_{\mathrm{aps}} \sim 1.2 \cdot \sqrt{R}$ mm by exploiting a circular distribution of PS located at a distance of R km from a target of interest. Then, for $R = 100$ m, we get 0.4 mm of dispersion, which would correspond to an SNR of 19 dB in C band. Keeping a margin of 3 dB leads to SNR $\sim$ 22 dB and then $\sigma_\phi \sim 5^\circ$.

Furthermore, the repeat-pass interferometry leads to consistent shifts in the images due to differences in orbit positioning during the same scene acquisition, particularly in range, and this has to be considered in "offset" tests like CEOS. The entity of range shift between images can be evaluated by considering that the orbit tube diameter for spaceborne SAR ranges from the 100 m for the next European Space Agency Sentinel-1 [21] to a diameter of 250 m for TerraSAR-X and even higher values for

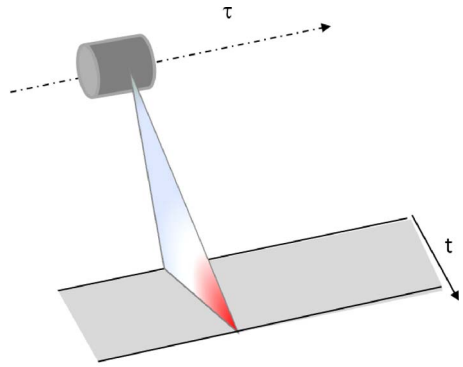

Fig. 2. Sketch of the acquisition geometry of the StripMAP mode.

COSMO-SkyMed and past missions (ERS and Envisat). These values lead to 60 slant range pixels in the Sentinel-1 case, to 250 pixels in TerraSAR-X by assuming the nominal 150-MHz bandwidth, or to 300 pixels by assuming the maximum bandwidth of 300 MHz for TerraSAR-X and COSMO-SkyMed [22]. Then, the 100-pixel shift of the CEOS test must be maintained, although higher values are desired.

III. Definition of the Acquisition Modes

The CEOS offset test was introduced for StripMAP, the sole operational mode in use at that time for spaceborne SAR. However, current systems exploit a wide variety of modes: ScanSAR [23], SPOTLIGHT [24], and TopSAR [25] will be considered here. Hybrid mode [26] and inverse TopSAR [27], [28] are less used, and they will not be explicitly considered here, although quite similar to SPOTLIGHT and TopSAR. Finally, dual polarization modes, like Envisat "Alternative Polarization" or COSMO-SkyMed "Ping-Pong" [29] are totally equivalent to ScanSAR mode, here discussed.

A. StripMAP

StripMAP is the default full-resolution SAR mode. The antenna footprint moves at the sensor speed along its trajectory without any steering. The footprint traces a swath in ground range on the Earth surface, producing images with a nominal azimuth resolution of $L_a/2$, where L_a is the physical antenna size. If the sensor trajectory is approximated with a straight line on a flat Earth or is a circular orbit over a spherical surface, the acquisition is geometrically invariant along the slow time axis (i.e., the azimuth axis).

The impulse response of a conventional SAR system, referring to the acquisition geometry sketched in Fig. 2, can be written as

$$h_{ST}(t,\tau;r) = G_a\left(\psi(\tau)\right) p\left(\tau - \frac{R(t,\tau;r)}{c}\right) \exp\left(-j\omega_0 \frac{R(t,\tau;r)}{c}\right) \quad (3)$$

where

t and τ	fast and slow time coordinates of the signal;
r	range coordinate of the target;
ω_0	carrier wavenumber;
c	light speed;

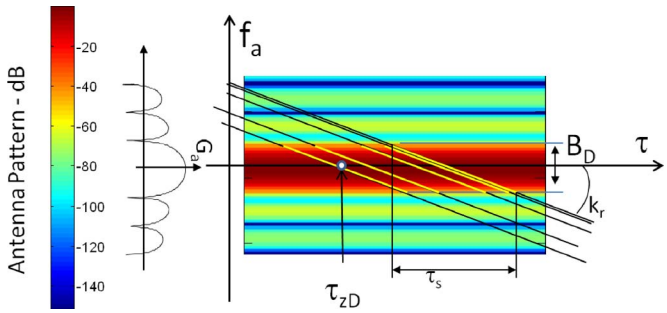

Fig. 3. AAP and the StripMAP data support in the slow time-Doppler domain. τ represents the slow time, f_a is the Doppler frequency, τ_{zD} is the zero Doppler time of the considered point target, τ_s is the time interval a point target spectrum takes to fall into the considered azimuth bandwidth B_D, and k_r is the frequency rate.

R	round trip distance covered by the wavefront and is two-way for monostatic SAR. Taking $\tau = \tau_0$ as the slow-time of nearest sensor-target approach, $R = \sqrt{[v_s(\tau - \tau_0)]^2 + r^2}$;
$\psi(\tau)$	squint angle under which the target is seen from the system;
G_a	overall gain of the system, which depends on the sensor speed v_s and on the closest approach distance r

$$G_a\left(\psi(\tau)\right) = G_0 \cdot \mathrm{sinc}^2\left(\frac{L_a}{\lambda}\psi\right) = G_0 \cdot \mathrm{sinc}^2\left(\frac{L_a}{\lambda}\frac{v_s\tau}{r}\right);$$

$p(t)$	transmitted pulse after range compression.

All of the targets at the same range from the sensor experience the same Doppler history which is modulated by the azimuth antenna pattern (AAP).

The data support in the slow time-Doppler domain for the StripMAP acquisition mode is shown in Fig. 3. The colors represent the AAP G_a, and the lines represent the instantaneous target spectrum as a function of the slow time τ. The spectrum is centered at the equivalent Doppler centroid frequency. The position of the point target is identified by the equivalent zero Doppler time $\tau_0 = \tau_{zD}$. Each target is seen by the antenna main lobe for a time τ_s, which is a function of the azimuth bandwidth B_D and frequency rate k_r. The ground coverage of a StripMAP acquisition mode is limited by physical and geometrical parameters such as the pulse repetition frequency, the antenna length, the wavelength, and the antenna offset from nadir.

From (3), it derives a range dependence of the IRF that requires that StripMAP focusing processors must process data with a range-variant compression function. It should also be noticed that the range history changes in slow time due to the curved orbit and Earth rotation. For this, the focusing kernel should be quite slowly variant in azimuth: Both features can be tested by the CEOS offset test.

B. ScanSAR and Alternate Polarization

ScanSAR is a SAR acquisition mode with a wider range swath coverage with respect to conventional StripMAP SAR systems [30]. This coverage is achieved by a progressive scanning of different subswaths: The antenna elevation angle is periodically switched in elevation in order to illuminate N

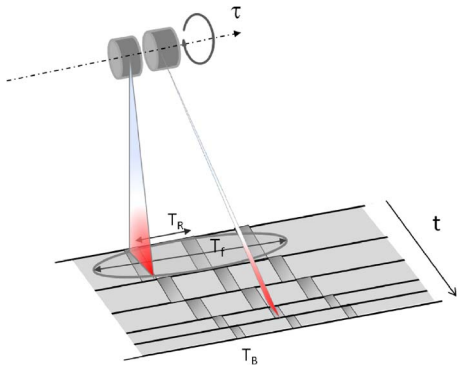

Fig. 4. ScanSAR mode acquisition geometry. The antenna beam is periodically switched in elevation to illuminate N range subswaths.

range subswaths on a time-division basis (see Fig. 4). Each burst of data is equivalent to a windowed portion of a StripMAP data set. The IRF for the nth subswath of a ScanSAR system can be written as [31]

$$h_{SC}(t,\tau;r) = h_{ST}(t,\tau;r) \cdot \sum_m \text{rect}\left(\frac{\tau - mT_R - nT_B}{T_B}\right) \quad (4)$$

where T_R is the burst cycle time and T_B is the burst length (we assume without loss of generality that the ScanSAR cycle is performed with n bursts of equal length). Due to the scanning effect, the antenna pattern for a single subswath is slowly time-varying for a ScanSAR system.

The acquisition scheme results in an imaged strip N times wider than that of a StripMAP SAR but also with an N times coarser azimuth resolution. Since the acquisition is obtained by sampling the scene with bursts, the scatterer contributions are differently collected according to their equivalent zero Doppler position. The impulse response, achieved by combining (3) and (4), approximating the range migration as quadratic and ignoring constant terms, is

$$\begin{aligned} h_{SC,n}(t,\tau;r) = {} & G_a\left(\psi(\tau)\right) p\left(\tau - \frac{R(t,\tau;r)}{c}\right) \\ & \cdot \exp\left(-j\pi k_a(\tau-\tau_0)^2\right) \\ & \cdot \sum_m \text{rect}\left(\frac{\tau - mT_R - nT_B}{T_B}\right) \end{aligned} \quad (5)$$

where

$$k_a = \frac{\omega_0}{2\pi c}\frac{\partial^2 R}{\partial \tau^2}.$$

The argument of the exponential is responsible for the instantaneous frequency

$$\begin{aligned} f_i &= \frac{1}{2\pi}\frac{\partial(\angle h_{SC})}{\partial \tau} \\ &= k_a(\tau - \tau_0) \; kT_R - nT_B \le \tau \le kT_R - (n+1)T_B \end{aligned} \quad (6)$$

which is common in any acquisition mode. For ScanSAR mode, however, the rectangular windowing makes available only spectral portions centered on frequency $k_a(mT_R - \tau_0)$ that depend on the burst time and on the target location τ_0. These spectral slices are weighted by the antenna pattern, as shown by the time–frequency diagram of Fig. 5. In the sample figure, each

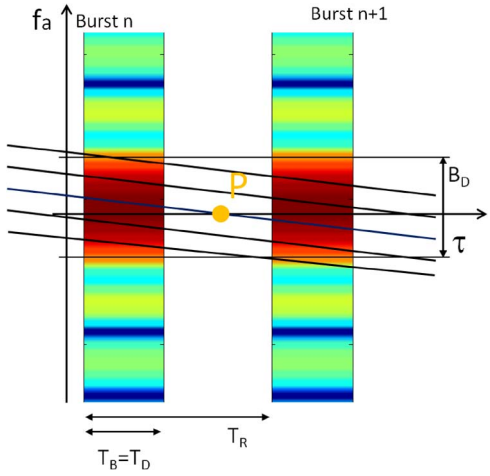

Fig. 5. ScanSAR data support for consecutive bursts of the same subswath in the slow time-Doppler domain. A wider ground coverage is obtained using periodic bursts with duration T_B and burst cycle time T_R. The zero Doppler position of a target is represented by the point P. The burst cycle time in the figure has been adjusted to correspond to two looks per target.

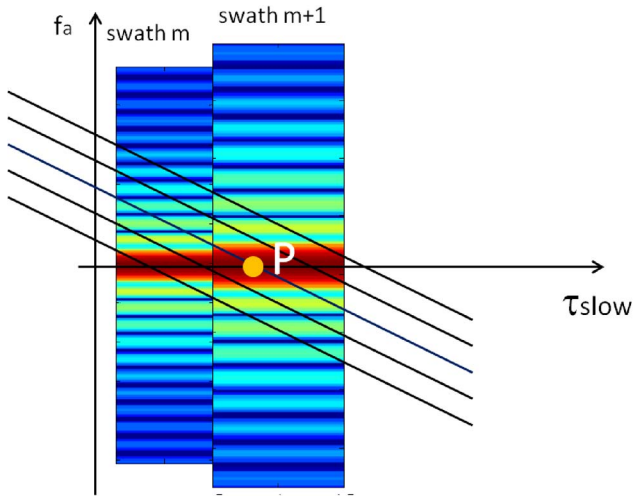

Fig. 6. Time-Doppler data support of a point target P in the overlap area of different (and adjacent) swaths for a ScanSAR acquisition. The burst length and the processed bandwidth are swath dependent.

subswath is illuminated for a time T_B with a T_R periodicity, and the system is dimensioned to have two different looks of each target. The raw data support of successive subswaths in the time-Doppler domain is reported in Fig. 6. The spectral support for a point target seen by successive swaths depends on the spectra of the two different swaths' antenna.

C. TopSAR

TopSAR is a SAR with a wider swath coverage in slant range with respect to conventional StripMAP SAR systems [25]. This swath coverage is achieved, like in the ScanSAR case, by scanning different subswaths, while the antenna look angle is switched into N different positions. Like in the ScanSAR mode, the ground coverage is enhanced by a factor N at the expense of the azimuth resolution. In both acquisition modes, in fact, each subswath is illuminated for a fraction of the total acquisition time, so the available azimuth bandwidth (inversely

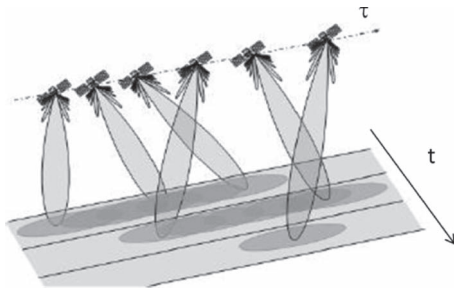

Fig. 7. TopSAR acquisition geometry. The antenna is steered both in range by dividing the swath in N subswaths like in ScanSAR and in azimuth by steering the antenna from backward to forward.

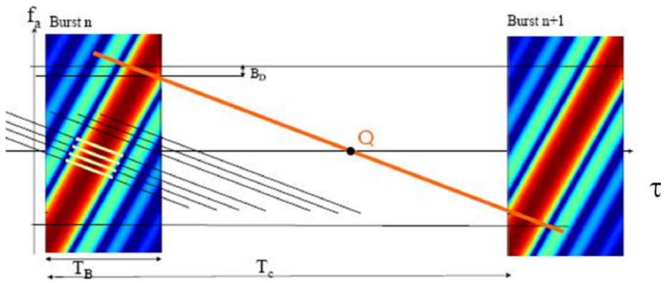

Fig. 8. Data support in the slow time-Doppler domain for the TopSAR mode. As in the ScanSAR acquisition mode, a wider ground coverage is achieved by exploiting bursts of length T_B and a burst repetition cycle T_c. Q represents the zero Doppler position of the considered point target. It is remarked that spectral support is time dependent also within the burst.

proportional to the resolution) is also a fraction of the full StripMAP case bandwidth.

In the TopSAR mode, the antenna is steered in both the azimuth and range directions: The antenna beam is steered during the acquisition of each burst from backward to forward, relative to the flight direction, achieving a larger azimuth bandwidth for all of the targets. The continuous coverage is achieved by sweeping the AAP cyclically. The resulting overall repeat cycle is much longer than that in the ScanSAR case since the area covered in each burst is larger, as shown by the geometrical sketch of the TopSAR acquisition mode in Fig. 7. The IRF of a TopSAR system can be written as follows:

$$h_{\mathrm{TOPS},n}(t,\tau;r) = G_{aT}\left(\psi(\tau)\right) p\left(\tau - \frac{R(t,\tau;r)}{c}\right) \cdot \exp\left(-j\omega_0 \frac{R(t,\tau;r)}{c}\right) \sum_m \mathrm{rect}\left(\frac{\tau - mT_R - nT_B}{T_B}\right). \quad (7)$$

The Doppler history of a given target is weighted by a reduced azimuth antenna aperture, as shown in Fig. 8, since each target is illuminated by a steered antenna footprint that is equivalent to the footprint of a fixed antenna shrunk by a factor α [25], [27]

$$\alpha = 1 - \frac{r \cdot \theta_\psi}{v_s} > 1 \quad (8)$$

where θ_ψ is the steering rate expressed as radians per second. It is worth to mention that the sign of the steering rate is negative for a backward-to-forward steering. The AAP becomes

$$G_{aT}\left(\psi(\tau)\right) = G_0 \cdot \mathrm{sinc}^2\left(\alpha \frac{L_a}{\lambda} \frac{v_s \tau}{r}\right). \quad (9)$$

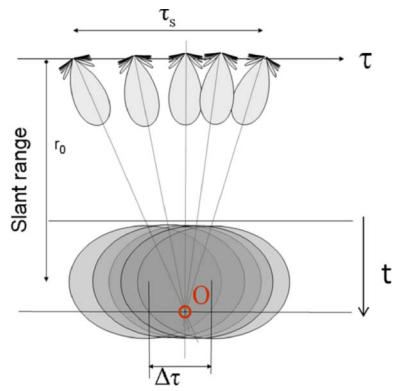

Fig. 9. SPOTLIGHT acquisition mode geometry. The antenna is steered from forward to backward, illuminating a selected target. This fact increases the azimuth resolution.

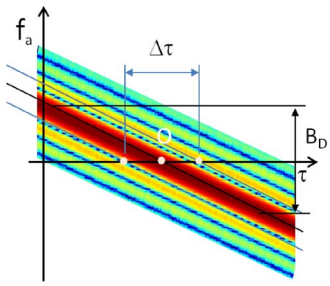

Fig. 10. Data support in the slow time-Doppler domain for the SPOTLIGHT acquisition mode. The main lobe of the antenna is steered to compensate the target Doppler rate illuminating the same target with the maximum SNR.

Each target Doppler history is illuminated by the same pattern of an equivalent StripMAP system where the antenna length is scaled by a factor α and the azimuth resolution is decreased of the same factor $\alpha L_a/2$ (see Fig. 8). Apart from this, spectral properties of TopSAR are very similar to ScanSAR. Data phase is subjected to a fast variation along azimuth due to the modulation introduced by the azimuth antenna steering.

D. SPOTLIGHT and Hybrid Modes

SPOTLIGHT is a SAR with an increased azimuth resolution [24]. The SPOTLIGHT acquisition scheme allows for the coverage of a limited area with a higher resolution without changing the system parameters. The increased azimuth resolution is achieved by steering the antenna to maintain the main lobe on the reference target (see Fig. 9). The beam is steered in the opposite direction with respect to the TopSAR mode: from forward to backward leading to a positive steering rate θ_ψ. Making reference to the geometrical scheme in Fig. 9, the IRF of the SPOTLIGHT mode can be written as [32]

$$h_{\mathrm{SPOT}}(t,\tau;r) = G_{aT}\left(\psi(\tau)\right) p\left(\tau - \frac{R(t,\tau;r)}{c}\right) \cdot \exp\left(-j\omega_0 \frac{R(t,\tau;r)}{c}\right). \quad (10)$$

Fig. 10 shows the data support in slow time-Doppler domain. Point O and the points in the dark gray region of Fig. 9 have an improved noise equivalent sigma zero since they are illuminated with the maximum of the antenna pattern and better geometric resolution due to the longer integration time.

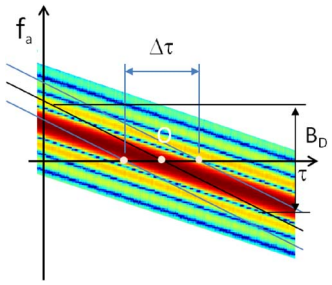

Fig. 11. Data support in the slow time-Doppler domain for the hybrid acquisition mode.

TABLE I
REQUIREMENTS TO BE SATISFIED

Name	Definition	Req.
BIAS	Mean of interferogram phase	$\leq 0.1^\circ$
STD	Standard deviation of interferogram phase	$\leq 5.5^\circ$
PBB	Phase discontinuity at the block boundary	$\leq 0.1^\circ$
PTD	Point Target phase difference of co-located targets	$\leq 5.5^\circ$

Hybrid modes are very similar to SPOTLIGHT acquisition, but the antenna steering is from forward to backward and does not compensate completely for the Doppler rate. In this way, the illuminated area with high resolution is increased with respect to the SPOTLIGHT mode at the expense of the azimuth resolution. Fig. 11 shows the data support in the slow time-Doppler domain.

IV. Test Definition

In this section, the different tests to be applied on focused data in order to verify the phase preservation are defined. The proposed tests can be divided in two different families. The first group is a set of self-consistent tests. The second group is a set of tests to be performed on the impulse response of isolated point targets in order to check the phase preservation of multiple swath/burst acquisition modes.

The overall pass/fail criteria for the tests, which have been derived from the requirements discussed in Section II, are reported in Table I. Four different requirements are derived: Phase bias (BIAS) and phase standard deviation (STD) measure the mean phase and standard deviation of the interferogram between two SLC images, and phase boundary block (PBB) aims at measuring the average discontinuity between focusing blocks. Point target difference (PTD) aims to measure the phase difference of a point target observed in multiple swaths/bursts.

The proposed tests are designed for SLC products; however, some of them can be extended to multilooked complex data.

A. Self-Consistent Tests

In this section, two complementary tests representing necessary conditions for phase preservation are introduced. The first one is an extension of CEOS offset test, as the classical CEOS is limited only to StripMAP data spectral support, and an extension is required to deal with the spectral support of non-StripMAP modes. The second one is a test sensitive to blocking artifacts that aims at verifying the phase requirements on block data. Some focusing algorithms that induce block phase artifacts can, in fact, pass the CEOS offset test without granting phase preservation, so this new test is introduced as additional complement.

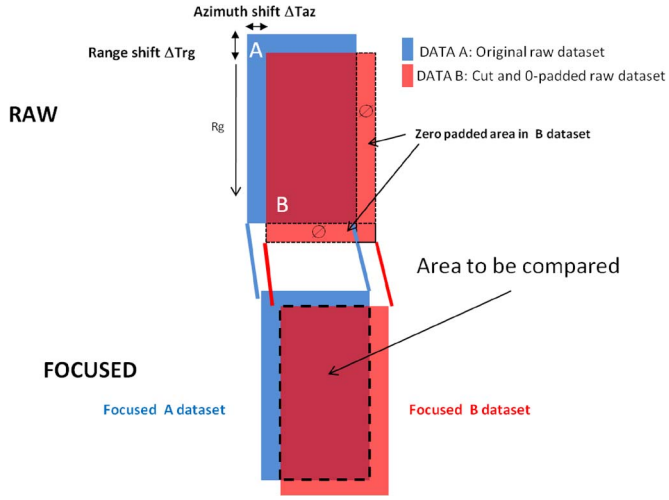

Fig. 12. Representation of the standard CEOS offset test.

1) Classical CEOS Offset Test: The CEOS offset test is the first and fundamental check to verify the phase preservation since it accounts for the space-variant nature of SAR focusing. The principle is that, if the input signal is **shifted** in the data domain (t, τ) and the focusing kernel is provided with the information of such shift in the model space, the result should be the same. Furthermore, as any space-invariant processor would pass the test, the requirement of "good focusing quality" is added. The test is performed as follows [2], [3]:

> Process two SLCs images from the same range-compressed raw data set and with the same trajectory, but with the start time offset by 100 lines in azimuth and 100 samples in range. The interferogram formed from these two properly coregistered SLCs images should ideally have a constant phase of zero and thus reveals possible processor induced artifacts.

The test is passed if, according to Table I, the requirements BIAS, STD, and PBB are satisfied in the overlap area between the two SLCs, as shown in Fig. 12. For testing purposes, the input raw data can be even pure complex noise with the same power spectrum of SAR data; the test is then a mean to verify focusing processor even in the absence of real data.

The typical value of shift used to verify the requirement is 100 pixel both in azimuth and range. The extent in range of the shift has been already discussed in Section II-B. In azimuth, it is agreed that the system synchronization is better than a shift of 100 pixel so that half this number could be used as well. The major problem in applying azimuth shift is, however, the "asynchronous scanning decorrelation" [31]. This problem is addressed and solved with the modified test proposed in the next section.

Eventually, the CEOS test does not specify a reference Doppler; however, it is wise to perform the test at the largest Doppler foreseen for the mission.

2) Extended CEOS Offset Test: The extended CEOS offset test is introduced to widen the pertinence of the standard CEOS test to all of the burst acquisition modes and to the acquisition modes in which the antenna is steered in the azimuth direction.

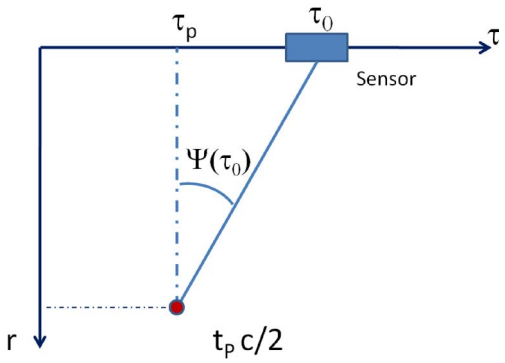

Fig. 13. Geometrical sketch of the angle between the point target and the sensor.

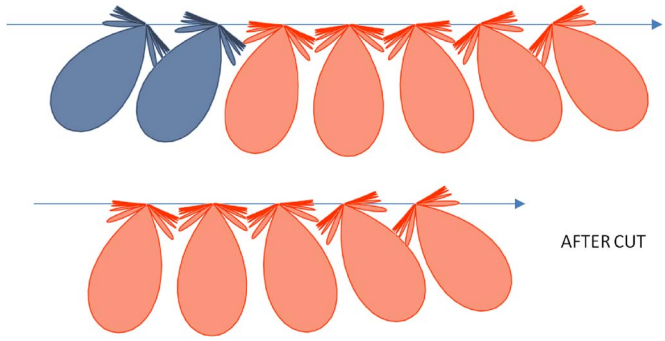

Fig. 14. Change in steering law and in antenna Doppler history due to the cut of some initial echoes for a TopSAR acquisition. The steering law is outlined in the picture.

The extended test consists in applying the standard CEOS offset on a filtered version of the SAR images. The filtering is performed on the raw data set by windowing the spectral contributions of those azimuth lines that are not present in both images.

The effect of applying the standard CEOS offset test on a burst acquisition mode is discussed, accounting for a ScanSAR acquisition mode (without loss of generality). As stated in Section III [see (4) and (5)], a single burst of a raw data set $d(t,\tau)$ can be written as follows:

$$d_{\mathrm{BURST}}(t,\tau) = d(t,\tau)\cdot \mathrm{rect}\left(\frac{\tau}{T_B}\right). \tag{11}$$

Let T_W be the azimuth length of the block chosen to perform the CEOS standard offset test. The two blocks of data used to perform the test can be expressed as

$$d_{\mathrm{CEOS}_1}(t,\ tau) = d_{\mathrm{BURST}}(t,\tau)\cdot \mathrm{rect}\left(\frac{\tau}{T_W}\right) \tag{12}$$

$$d_{\mathrm{CEOS}_2}(t,\tau) = d_{\mathrm{BURST}}(t,\tau)\cdot \mathrm{rect}\left(\frac{\tau - n\cdot d\tau}{T_W}\right) \tag{13}$$

where $d\tau$ is the azimuth time sampling interval and n is the applied offset between the two images. We chose, for sake of simplicity, the CEOS window as long as a burst duration ($T_W = T_B$). Referring to Fig. 13, the instantaneous wavenumber observed by the sensor is

$$k_\tau = \frac{\omega+\omega_0}{c}\sin\psi(\tau) \simeq \frac{\omega+\omega_0}{c}\frac{\tau}{t_P}. \tag{14}$$

The spectral contribution of a target at $(\tau_P = 0, t_P)$ when the data are windowed as in (12) ranges in $[k_{\tau_{\min}}, k_{\tau_{\max}}]$, where

$$\begin{aligned} k_{\tau_{\min_1}} &= 0 \\ k_{\tau_{\max_1}} &= \frac{\omega+\omega_0}{c}\frac{T_B}{t_P}. \end{aligned} \tag{15}$$

On the other hand, the spectral contribution of $d_{\mathrm{CEOS}_1}(t,\tau)$ is wider as it is limited only by the antenna footprint.

When the data are windowed as in (13), for $d_{\mathrm{CEOS}_2}(t,\tau)$, the spectral contribution of the target changes within the interval of extremes

$$\begin{aligned} k_{\tau_{\min_2}} &= \frac{\omega+\omega_0}{c}\frac{n\cdot d\tau}{t_P} \\ k_{\tau_{\max_2}} &= \frac{\omega+\omega_0}{c}\frac{T_B}{t_P} \end{aligned} \tag{16}$$

while the spectral contribution of $d_{\mathrm{CEOS}_2}(t,\tau)$ is the same as $d_{\mathrm{CEOS}_1}(t,\tau)$ since the antenna footprint does not change, being based on the same acquisition geometry.

The difference between $k_{\tau_{\min_1}}$ and $k_{\tau_{\min_2}}$ in (15) and (16) implies that, when we compute the interferogram, there is a portion of the data spectrum that is not common to both images. This introduces a phase noise that is not dependent on the processor.

For this reason, some changes in the CEOS test are introduced in order to extend its applicability to the burst acquisition modes. This is obtained by nulling the first and the last n lines of the two raw data sets taken into consideration, respectively. The test is then reformulated as follows:

> Consider two blocks of the same range compressed raw data set, acquired with the same trajectory, but offset by n azimuth lines and m range samples. Process the first block of data after setting to zero its first n azimuth lines and its first m range samples and process the second one after updating the Doppler centroid according to the acquisition law (with respect to the first block) and setting to zero its last n azimuth lines and its last m range samples. The interferogram formed from these two properly co-registered SLCs images should ideally have a constant phase of zero and thus reveals possible processor induced artifacts.

The change of Doppler centroid is required if the azimuth central frequency varies fast along the azimuth direction like in the TopSAR case where the antenna steering induces large changes in the antenna pointing and so in data spectrum.

Fig. 14 represents with a schematic plot the change of the steering law and consequently of the Doppler centroid due to the cut of n echoes of the first image for a TopSAR acquisition. The starting Doppler centroid changes as a function of the timeline of the acquisition and can be expressed as

$$\mathrm{DC} = \mathrm{DC}_0 - 2\frac{v_s}{\lambda}\sin\ \frac{n}{\mathrm{PRF}}\theta_\psi \tag{17}$$

where DC_0 is the initial Doppler centroid frequency, v_s is the sensor velocity, PRF is the pulse repetition frequency, and θ_ψ is the angular antenna sweep velocity.

The test is passed with the same requirements of the standard CEOS offset test, i.e., if the requirements BIAS, STD, and PBB are satisfied in the overlap area between the two SLCs

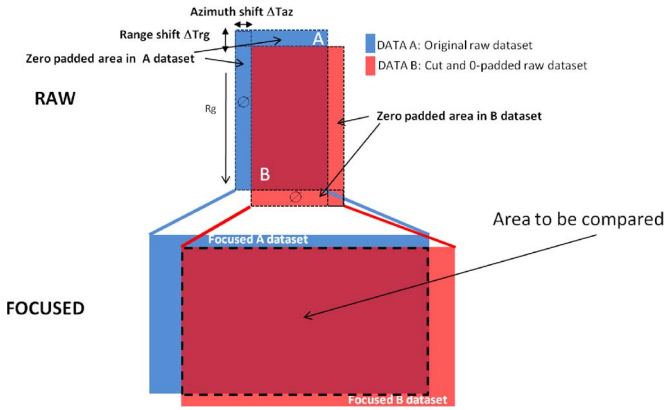

Fig. 15. Representation of the modified CEOS offset test.

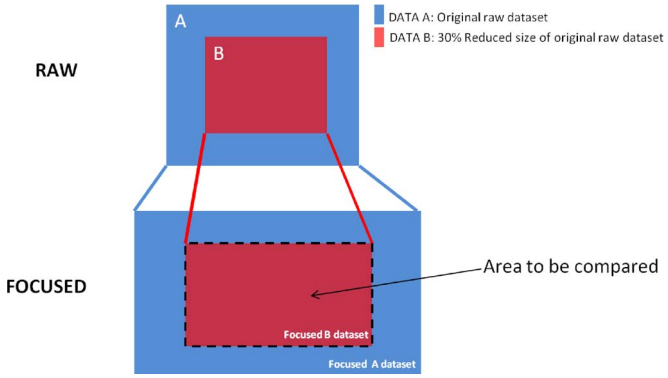

Fig. 16. Representation of the size block test.

according to Table I. Also, in this case, it is wise to perform the test at the maximum Doppler foreseen for the mission. A schematic representation of the extended CEOS offset test is reported in Fig. 15.

3) Size Block Test: In the implementation of many SAR processors, the transfer function is approximated in blocks; it keeps constant throughout the whole block and minimizes the errors (apart for slight increasing at block edges) by a suitable overlap. The size block test has been introduced to check the consistency of the processor when blocks of different sizes are exploited, even if the data are not shifted at all. Therefore, such test, somewhat complementary to CEOS offset, checks the consistency versus different shifts for blocks of the same size. The union of the two tests increases the robustness of the validation.

The test should be performed as follows:

> Consider two blocks of the same raw data set, acquired with the same trajectory. One of the block has different size with respect to the other: 30% more for both range and azimuth lengths. The interferogram formed by the two blocks after processing and properly co-registering should ideally have a constant phase of zero and thus reveals possible processor induced artifacts.

Also, in this case, the mean and standard deviation of the phase interferogram in the common region between the SLC data (red region in Fig. 16) are taken into account. The pass/fail criteria to be satisfied are the same as those of the CEOS test: BIAS, STD, and PBB (see Table I).

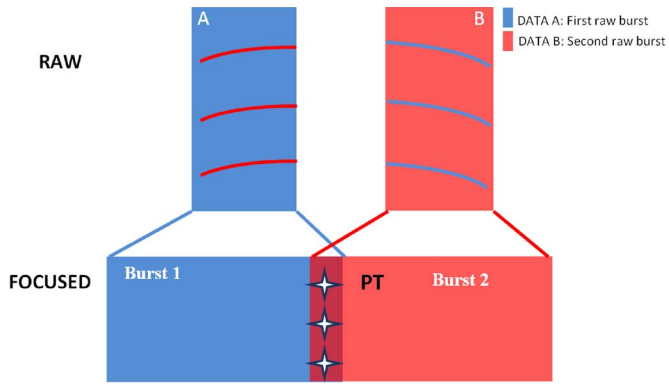

Fig. 17. (Top) Representation of the point target amplitude in two adjacent bursts in raw data (see also Fig. 5 for the same representation in the spectral domain). (Bottom) Representation of the point target positions in two adjacent bursts belonging to the same swath in the focused data domain. The dark red region is the area viewed by both bursts.

B. Point Target Tests

It has been stated that the "consistent" tests, although necessary, are not a set of sufficient conditions for phase requirements. A case to be checked with attention is the mosaicking in burst-mode processors, as it happens that targets in very close positions are processed by very different processing parameters. This is the case of the overlap area between adjacent bursts and swaths. As described in Section III-B and C, the overlap area is a very narrow portion of the antenna footprint both in the azimuth and range directions. The test aims at verifying that the phase of point-like targets is the same in different bursts, although their spectral support is changed. These sets of tests require simulated data sets containing only isolated point-like stable targets in such overlap portions of the antenna footprint. True data sets with real point targets placed in the overlap regions can also be used; however, such test is not recommended. In fact, many artifacts affect real data, like ambiguities, oscillator jitter, and tropospheric and ionospheric disturbances, besides the nonideality of the targets themselves, which would suggest relaxing of the quantitative requirements. The point target phase quality should be within the one foreseen in the mission requirements.

The phase of each point target accounted in the test is measured as the phase of the 2-D IRF associated to the point target at the correct zero Doppler position. The absolute value of the difference between the measured phase is taken into account in the test.

1) Interburst Point Target Test: The interburst point target test is introduced to verify the consistency of the focusing kernel applied to a burst acquisition mode. This test is based on the analysis of the point spread function of isolated point scatterers. We consider a raw data set containing some isolated point targets (PT) with different range positions seen by two successive bursts, and we compare the phase of these focused targets. The position of the targets is chosen in order to assure a reasonable separation between the response functions (see Fig. 17). The aim of this test is to verify that the same target phase is obtained by processing different spectral contributions of the same point scatterer.

The test should be performed as follows:

Consider a raw SAR data set composed of two consecutive bursts. The scenario is composed by some isolated and stable point targets positioned in the overlap area between the bursts. Process the two raw images and consider the SLCs obtained. The phase of the focused point targets should be the same in the two images. Phase differences reveal possible processor induced artifacts.

The pass/fail criterion for this test is PTD (see Table I), based on the measure of the point target phase difference.

2) Interswath Point Target Test: The interswath point target test is introduced to test the phase performances of the processor applied on different swaths. This test is based on the analysis of the point spread function of some isolated point targets (PT) as in the previous test.

Let us simplify the ScanSAR impulse response in (6), for a single target in τ_0 and a single burst starting at $\tau = T$ as the 1-D signal

$$h_{SC}(\tau;\tau_0) = \exp\left(j\pi k_a(\tau-\tau_0)^2\right) \quad T < \tau < T + T_B.$$

The focused signal, achieved after convolution by the SAR matched reference, is

$$\begin{aligned} s(\tau) &= h_{SC}(\tau;\tau_0) * \underset{T+T_B}{\exp(j\pi k_a \tau^2)} \\ &= \int_T \exp\left(-j\pi k_a(\rho-\tau-\tau_0)^2\right)\exp(j\pi k_a\rho^2)d\rho \end{aligned}$$

where

$$k_a = \frac{\omega_0}{2\pi c}\frac{\partial^2 R}{\partial \tau^2}.$$

Eventually, we get

$$\begin{aligned} s(\tau) = \exp\left(-j\pi k_a(\tau-\tau_0)^2\right)\cdot\exp\left(j2\pi k_a(\tau-\tau_0)T_B\right) \\ \times \operatorname{sinc}\left(k_a(\tau-\tau_0)\cdot\left(T+\frac{T_B}{2}\right)\right). \end{aligned} \quad (18)$$

The three terms correspond to the following:

1) a residual phase curvature that comes from the sensor-target distance and cannot be removed;
2) a frequency shift that depends on the relative target position within the burst τ_0;
3) the amplitude of the focused IRF, which is a sinc pulse.

Notice that, for $\tau = \tau_0$, the phase is zero whatever the burst window time is. This means that the phase of the same target focused by different bursts is exactly the same if it is evaluated precisely in the nominal target location. Nonetheless, in a very small neighborhood of that location, the phase has a ramp that depends on both the target azimuth location and the burst. The residual term coming from two different swaths is, from (18)

$$\begin{aligned} s(\tau;T_1)\cdot s^*(\tau;T_2) = \exp\left(-j2\pi k(\tau-\tau_0)(T_1-T_2)\right) \\ \times \operatorname{sinc}^2\left(k_a(\tau-\tau_0)\cdot T_B\right). \end{aligned} \quad (19)$$

This term could affect the phase evaluation and could cause the interpolation in the nominal target location to introduce a small error. Therefore, the IRF should be deramped by the second exponential term in (18), which requires *a priori* knowledge of τ_0, well known in case of simulated data or transponder.

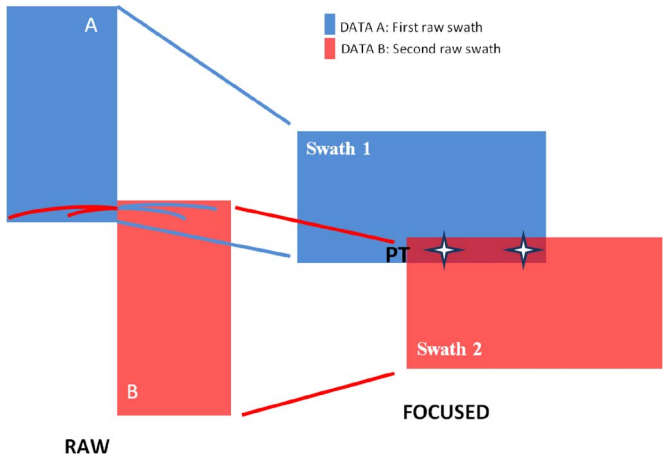

Fig. 18. (Left) Representation of the point target amplitude in two adjacent swaths in raw data. See also Fig. 6 for the same representation in spectral domain. (Right) Representation of the point targets position in two adjacent swaths in focused data domain. The dark red region is the area viewed by both swaths.

The test is performed by processing PTs seen by two successive swaths, deramping each swath and comparing the phase of the focused scatterers as represented in Fig. 18. The test should be performed as follows:

Generate a raw SAR data set composed by two different bursts of data looking at the same scenario with the same trajectory but with different elevation angles (different swaths). The scene includes some isolated and stable point targets positioned in the overlap area between the swaths. Process the two raw images and deramp at zero Doppler the results. The phase of the simulated point targets should ideally be the same in the two images. Phase differences thus reveal processor induced artifacts.

The pass/fail criterion of this test is the same as that of the interburst point target test: The scatterer phase must satisfy the requirement PTD (see Table I). Note that the pass fail criterion of the interswath PT test is more stringent to be satisfied as different pulse repetition frequencies and different sampling frequencies can be set in different swaths. It is recommended to resample the different swaths on a common grid prior to performing the test.

V. Test Pertinence

In this section, the applicability of each test to the defined acquisition modes is discussed. Table II illustrates how the different tests map to the acquisition modes considered in this paper. The burst acquisition modes are split in two columns: one to discuss the applicability of the tests inside the same burst and the other to discuss the applicability of the tests in successive bursts or swaths. In the table, we indicate for each column if the tests can be applied successfully or not to the corresponding acquisition mode.

A. StripMAP Mode

All of the self-consistent tests proposed (CEOS test, extended CEOS test, and size block test) are successfully applicable to data sets acquired with the StripMAP mode. Obviously, none of the interburst/interswath tests is applicable to StripMAP data sets.

TABLE II
APPLICABILITY MATRIX OF THE TESTS

	StripMAP	ScanSAR		TopSAR		SPOTLIGHT
		Intra burst/swath	Inter burst/swath	Intra burst/swath	Inter burst/swath	
CEOS	✓	×	×	×	×	✓
Extended CEOS	✓	✓	×	✓	×	✓
Size block	✓	✓	×	✓	×	✓
Inter burst PT test	×	×	✓	×	✓	×
Inter swath PT test	×	×	✓	×	✓	×

B. ScanSAR Mode

The applicability of the tests for the ScanSAR mode is divided in two different subsections: intraburst test applicability and interburst/interswath test applicability. The size block test and the extended CEOS test can be applied to intraburst data, while the standard CEOS test cannot be applied due to the lack of common spectra in the data. All of the PT test defined can be applied to interburst/interswath ScanSAR data.

C. TopSAR Mode

The applicability of the tests for the TopSAR mode is also divided in two different subsections: intraburst applicability and interburst/interswath applicability. The size block test and the extended CEOS test can be applied to intraburst data, while the standard CEOS test cannot be applied. All of the PT tests can be applied to interburst/interswath TopSAR data.

D. SPOTLIGHT Mode

The SPOTLIGHT acquisition mode acquires data within a single burst/single swath, so all the point target tests are not applicable. The size block test and standard and extended CEOS offset tests are all applicable to this acquisition mode.

VI. CONCLUSION

This paper has proposed a novel set of tests aim at measuring the phase preservation of SAR focusing processors, covering the majority of the acquisition modes. In particular, two categories are introduced: 1) self-consistent tests, which extend the applicability of CEOS test to non-StripMAP acquisition modes, and 2) the size block tests, introduced to reveal artifacts not otherwise detectable. Point target tests have been introduced to check the consistency of focusing across different swaths/bursts. The tests can be applied to any processor, either based on time or frequency domain kernels and to a wide variety of systems (i.e., airborne, spaceborne, ground-based, monostatic, and bistatic systems), thus providing a complete and generic tool for the quantitative evaluation of the phase-preserving performance of SAR processors. Each test must be passed, satisfying some constraints derived by interferometric requirements on the phase also discussed in this paper. We suggest the use of these tests as a tool to provide quantitative comparison and to evaluate the performance of any SAR focusing algorithm.

ACKNOWLEDGMENT

The authors would like to thank Prof. F. Rocca and Dott. F. de Zan for the analysis reported in Section II.

REFERENCES

[1] R. Keith Raney and P. W. Vachon, "A phase preserving SAR processor," in *Proc. 12th Can. Symp. Remote Sens. Geosci. Remote Sens. Symp.*, vol. 1, *Quantitative Remote Sensing: An Economic Tool for the Nineties, Volume 1*, 1989, pp. 2588–2591.

[2] R. Bamler and B. Schaettler, "Phase-Preservation in SAR Processing: Definition, Requirements and Tests," DLR Technology, Owings Mills, MD, USA, DLR Tech. Note Ver 1.0, May 1995.

[3] B. Rosich Tell and H. Laur, "Phase preservation in SAR processing: The interferometric offset test," in *Proc. Int. Geosci. Remote Sens. Symp.*, Lincoln, NE, USA, May 27–31, 1996, pp. 477–480.

[4] S. Coulson and F. Rocca, "Summary report of working group 4: Interferometric SAR calibration," in *Proc. CEOS SAR Workshop*, 1993, pp. 376–379.

[5] A. Barmettler, P. Pasquali, D. Small, and D. Nuesch, "Cross-compatibility of ERS-SLC products," in *Proc. FRINGE Workshop ERS SAR Interferometry*, Zürich, Switzerland, Sep. 30–Oct. 2, 1996.

[6] A. Monti Guarnieri and P. Guccione, "Optimal focusing for low resolution ScanSAR," *IEEE Trans. Geosci. Remote Sens.*, vol. 39, no. 3, pp. 479–491, Mar. 2001.

[7] "Quality Measurements Definition for ASAR Level 1 Products," European Space Agency (ESA), Paris, France, Tech. Rep., Mar. 2002.

[8] M. Belotti, D. D'Aria, L. Iannini, A. Monti Guarnieri, and S. Scirpoli, "Phase requirements for the validation of phase preserving processors for spaceborne SAR systems," in *Proc. ESA Living Planet Symp.*, Bergen, Norway, 2010, pp. 1–39.

[9] M. Belotti, D. D'Aria, L. Iannini, A. Monti Guarnieri, and S. Scirpoli, "Phase requirements, design and validation of phase preserving processors for a SAR system," in *Proc. IEEE IGARSS*, 2011, pp. 4095–4098.

[10] A. Monti Guarnieri and S. Tebaldini, "Hybrid Cramér–Rao bounds for crustal displacement field estimators in SAR interferometry," *IEEE Signal Process. Lett.*, vol. 14, no. 12, pp. 1012–1015, Dec. 2007.

[11] D. Just and R. Bamler, "Phase statistics of interferograms with applications to synthetic aperture radar," *Appl. Opt.*, vol. 33, no. 20, pp. 4361–4368, Jul. 1994.

[12] M. Cattabeni, A. Monti Guarnieri, and F. Rocca, "Estimation and improvement of coherence in SAR interferograms," in *Proc. Int. Geosci. Remote Sens. Symp.*, Pasadena, CA, USA, Aug. 8–12, 1994, pp. 720–722.

[13] G. Krieger, A. Moreira, H. Fiedler, I. Hajnsek, M. Werner, M. Younis, and M. Zink, "TanDEM-X: A satellite formation for high-resolution SAR interferometry," *IEEE Trans. Geosci. Remote Sens.*, vol. 45, no. 11, pp. 3317–3341, Nov. 2007.

[14] D. Moller, S. Hensley, G. A. Sadowy, C. D. Fisher, T. Michel, M. Zawadzki, and E. Rignot, "The glacier and land ice surface topography interferometer: An airborne proof-of-concept demonstration of high-precision Ka-band single-pass elevation mapping," *IEEE Trans. Geosci. Remote Sens.*, vol. 49, no. 2, pp. 827–842, Feb. 2011.

[15] F. Rocca, "Modeling interferogram stacks," *IEEE Trans. Geosci. Remote Sens.*, vol. 45, no. 10, pp. 3289–3299, Oct. 2007.

[16] H. Rott, B. Scheuchl, A. Siegel, and B. Grasemann, "Monitoring very slow slope movements by means of SAR interferometry: A case study from a mass waste above a reservoir in the Ötztal Alps, Austria," *Geophys. Res. Lett.*, vol. 26, no. 11, pp. 1629–1632, Jun. 1999.

[17] A. Ferretti, C. Prati, and F. Rocca, "Permanent scatterers in SAR interferometry," in *Proc. IEEE Int. Geosci. Remote Sens. Symp.*, Hamburg, Germany, Jun. 28–Jul. 22, 1999, pp. 1528–1530.

[18] R. F. Hanssen, *Radar Interferometry: Data Interpretation and Error Analysis*. Dordrecht, The Netherlands: Kluwer, 2001.
[19] L. Iannini and A. Monti Guarnieri, "Atmospheric phase screen in ground-based radar: Statistics and compensation," *IEEE Geosci. Remote Sens. Lett.*, vol. 8, no. 3, pp. 537–541, May 2011.
[20] A. Rucci, A. Ferretti, A. Monti Guarnieri, and F. Rocca, "Sentinel 1 SAR interferometry applications: The outlook for sub millimeter measurements," *Remote Sens. Environ.*, vol. 120, pp. 156–163, May 2012.
[21] "GMES Sentinel-1 System Requirements Document," European Space Agency (ESA), Paris, France, Tech. Rep., Jun. 2006.
[22] A. Torre, D. Calabrese, and M. Porfilio, "COSMO-SkyMed: Image quality achievements," in *Proc. 5th Int. Conf. RAST*, Jun. 2011, pp. 861–864.
[23] A. Currie and M. A. Brown, "Wide-swath SAR," *Proc. Inst. Elect. Eng.—F*, vol. 139, no. 2, pp. 123–135, Apr. 1992.
[24] W. G. Carrara, R. S. Goodman, and R. M. Majewski, *Spotlight Synthetic Aperture Radar: Signal Processing Algorithms*. Boston, MA, USA: Artech House, 1995.
[25] F. De Zan and A. Monti Guarnieri, "TopSAR: Terrain observation by progressive scans," *IEEE Trans. Geosci. Remote Sens.*, vol. 44, no. 9, pp. 2352–2360, Sep. 2006.
[26] D. P. Belcher and C. J. Baker, "High resolution processing of hybrid strip-map/spotlight mode SAR," *Proc. Inst. Elect. Eng.—Radar Sonar Navig.*, vol. 143, no. 6, pp. 366–374, Dec. 1996.
[27] D. D'Aria, F. De Zan, D. Giudici, A. Monti Guarnieri, and F. Rocca, "Burst-mode SARs for wide-swath surveys," *Can. J. Remote Sens.*, vol. 33, no. 1, pp. 27–38, Feb. 2007.
[28] A. Meta, J. Mittermayer, P. Prats, R. Scheiber, and U. Steinbrecher, "TOPS imaging with TerraSAR-X: Mode design and performance analysis," *IEEE Trans. Geosci. Remote Sens.*, vol. 48, no. 2, pp. 759–769, Feb. 2010.
[29] F. Caltagirone, G. De Luca, F. Covello, G. Marano, G. Angino, and M. Piemontese, "Status, results, potentiality and evolution of COSMO-SkyMed, the Italian earth observation constellation for risk management and security," in *Proc. IEEE IGARSS*, Jul. 2010, pp. 4393–4396.
[30] R. K. Moore, J. P. Claassen, and Y. H. Lin, "Scanning spaceborne synthetic aperture radar with integrated radiometer," *IEEE Trans. Aerosp. Electron. Syst.*, vol. AES-17, no. 3, pp. 410–420, May 1981.
[31] A. Monti Guarnieri and C. Prati, "ScanSAR focusing and interferometry," *IEEE Trans. Geosci. Remote Sens.*, vol. 34, no. 4, pp. 1029–1038, Jul. 1996.
[32] C. Prati, A. Monti Guarnieri, and F. Rocca, "SPOT mode SAR focusing with the $\omega - k$ technique," in *Proc. Int. Geosci. Remote Sens. Symp.*, Espoo, Finland, Jun. 3–6, 1991, pp. 631–634.